

**A Janus Protein-based Nanofabric for Trapping Polysulfides
and Stabilizing Lithium Metal in Lithium-Sulfur Batteries**

Journal:	<i>Journal of Materials Chemistry A</i>
Manuscript ID	TA-ART-02-2020-001989.R2
Article Type:	Paper
Date Submitted by the Author:	22-Mar-2020
Complete List of Authors:	Chen, Min; Washington State University; Chongqing University Chen, Zhiping; Chongqing University Fu, Xuewei; Washington State University, School of Mechanical and Materials Engineering Zhong, Wei-Hong; Washington State University, Mechanical and Materials Engineering

A Janus Protein-based Nanofabric for Trapping Polysulfides and Stabilizing Lithium Metal in Lithium-Sulfur Batteries

Min Chen, Zhiping Chen, Xuewei Fu, Wei-Hong Zhong***

M. Chen, Dr. X. W. Fu
School of Mechanical and Materials Engineering, Washington State University, Pullman, WA
99164, USA
E-mail: Xuewei.fu@wsu.edu (Dr. X. W. Fu)

M. Chen, Dr. Z. P. Chen
College of Materials Science and Engineering, Chongqing University, 174 Shazhengjie,
Chongqing, 400044, China

Prof. W. H. Zhong
School of Mechanical and Materials Engineering, Washington State University, Pullman, WA
99164, USA
E-mail: katie_zhong@wsu.edu (Prof. W.H. Zhong)

Abstract

The shuttling of polysulfides and uncontrollable growth of lithium dendrites remain the most critical obstacles deteriorating the performance and safety of lithium-sulfur batteries. Separator plays a key role in molecule diffusion and ion transport kinetics; thus, endowing the separator with functions to address the above two issues is in urgent need. Herein, a protein-based, low-resistance Janus nanofabric is designed and fabricated for simultaneously trapping polysulfides and stabilizing lithium metal. The Janus nanofabric is achieved via combining such two functional nanofabric layers: gelatin-coated conductive nanofabric (G@CNF) as a polysulfide-blocking layer and gelatin nanofabric (G-nanofabric) as an ion-regulating layer into a heterostructure. The gelatin-coating of G@CNF effectively enhances the polysulfide-trapping ability owing to strong gelatin-polysulfide interactions. The G-nanofabric with exceptional wettability, high ionic conductivity ($4.9 \times 10^{-3} \text{ S cm}^{-1}$) and high lithium-ion transference number (0.73) helps stabilize ion deposition and thus suppresses the growth of lithium dendrites. As a result, the Li/Li symmetric cell with G-nanofabric delivers ultra-long cycle life for over 1000 h with very stable performance. Benefiting from the synergistic effect from the two functional layers of the Janus nanofabric, the resulting Li-S batteries demonstrate excellent capacity, rate performance and cycle stability (e.g. initial discharge capacity of 890 mAh g^{-1} with a decay rate of 0.117% up to 300 cycles at 0.5 A g^{-1}).

Keywords: Janus nanofabric, gelatin, ion deposition, shuttle effect, Li-S batteries

Introduction

With the ever-increasing demand for advanced energy storage systems, numerous efforts have been contributed to developing electrochemical storage devices including rechargeable batteries, supercapacitors, fuel cells, etc. Among these, supercapacitors have high power density, but their energy density is limited^{1, 2}; lithium-ion batteries have gain great commercialization success, yet the theoretical energy limits make them hardly able to support high-demanding need^{3, 4}. Recently, lithium-sulfur (Li-S) batteries have been capturing extensive witnesses and research enthusiasm due to their high theoretical energy density (2600 Wh kg⁻¹) and the low cost of sulfur, which is a promising candidate for high-energy storage device with a reduced cost.^{5, 6} However, the practical application of Li-S batteries is still hindered by several intractable challenges from the intrinsic properties and electrochemistry of the active materials. One of the predominant problems is the shuttling of soluble intermediate polysulfides between sulfur cathode and lithium anode, i.e. shuttle effect, which results in irreversible loss of sulfur active materials, low Coulombic efficiency and quick capacity degradation.^{7, 8} To inhibit the shuttle effect, many strategies have been proposed, including rational design of sulfur host materials (conductive polymers⁹, nano-carbon^{10, 11} and graphene oxide¹²⁻¹⁵, metal oxides^{16, 17}), modification of electrolyte components¹⁸ or employment of solid electrolytes¹⁹, as well as engineering of separators²⁰. These efforts have made significant progress for improving the performance of the batteries; however, the growth of Li dendrites remains another critical issue in Li-S batteries, which may severely shorten the cycle life, and the overgrowing may penetrate through the separator, resulting in internal circuit and even explosion and fires.

Besides the studies of resolving the shuttle effect, stabilizing Li metal becomes increasingly important today to realize a high-performance and safe Li-S battery. To achieve that, people have

attempted various methods such as optimization of electrolyte components^{21, 22}, creation of artificial solid electrolyte interphase (SEI)^{23, 24}, introduction of 3D scaffolds^{25, 26}, and modification of separators. It is known that the nonuniform deposition of Li ions is the origin initiating the formation of lithium dendrites^{27, 28}. Separator, as a key interfacial component linking S cathode and Li anode, plays a crucial role in molecule diffusion and ion-deposition kinetics. Therefore, it is expected that engineering of separators has great potential to synchronously address the two critical issues, shuttle effect and dendritic Li growth, leading to improvement in battery performance and safety.

Intensive research has endowed the separators with ability of capturing polysulfides and/or suppressing the growth of Li dendrites. To reduce the shuttle effect, the modified separators or interlayers are supposed to be able to strongly trap polysulfides and to be electrical conductive, thus leading to reduced polysulfide diffusion and improved sulfur utilization.²⁹ Thus far, various materials that can anchor polysulfides and electrically conductive materials have been employed to fabricate interlayers, including polar polymers functionalized carbon materials³⁰, metal oxide/carbon composites³¹, metal oxide/metal nitride heterostructure³², conductive metal–organic frameworks (MOFs)^{33, 34}, etc. Specifically, due to the vast variety of polar groups, biomaterials have also been applied to trap polysulfides recently, including various polysaccharides (gum arabic³⁵, chitosan³⁶, etc.) and proteins (gelatin³⁷, soy protein³⁸, etc.), which has been summarized in previous study³⁹. Meanwhile, with the aim of stabilizing Li metal, efforts have been primarily concentrated on creating ion-flux redistributor on the separator, such as N-/S-doped graphene nanosheets (NSG)⁴⁰, boron-nitride (BN) nanosheets⁴¹, LiNO₃/Al₂O₃/PVDF⁴², XC72 carbon black interlayer⁴³, etc. Impressively, some separators modified with functional layer on both surfaces are able to simultaneously prohibit the shuttling of polysulfides and growth of Li dendrites. As of this

strategy, polypyrrole⁴⁴, carbon nanotubes⁴⁵, etc. have been adopted on both sides of the separators, which not only prevented the migration of polysulfides but also guided uniform Li ion flux. Although the dual-layer functionalized separators were effective in tackling the two critical issues in Li-S batteries, the substantial increase of thickness/mass brought from the added functional layers on the separator inevitably increased the ion-transport resistance and even sacrificed the battery energy density. To overcome this issue, therefore, design of advanced and dual-functional separators with low ion-transport resistance is strongly needed.

Based on the above considerations, instead of fabricating dual-layer functionalized separators, creation of Janus separators represents a feasible and appealing configuration. The Janus configuration consisting of two parallel functional materials avoids the addition of two functional layers to a conventional separator, thus reducing the ion-transport resistance. For example, Kong, et al.⁴⁶ reported a Janus separator with a carbon nanofiber (CNF) layer toward sulfur cathode and polyimide (PI) nanofabric toward Li metal anode, which could trap and convert the polysulfides, and promote the Li⁺ transport. The polyvinylpyrrolidone (PVP) coated-CNF has dipole-dipole interaction with polysulfides, while the excellent wettability with electrolyte and the highly porous structure of PI nanofibers ensure fast ion transport. A Janus cation exchange membranes consisting of an ultrathin ion-selectivity dense layer and a microporous supporting layer was fabricated with sulfonated poly (ether ether ketone) (SPEEK), which could effectively sieve the ions with low resistance for Li⁺ transfer.⁴⁷ In spite of the progress, the inability of these Janus separators for stabilizing Li metal remains a critical drawback, limiting the further improvement in the long-term performance of the resulting batteries.

To address the above issue, herein, we report a protein-based, low-resistance Janus nanofabric separator capable of trapping polysulfides and stabilizing Li metal. The Janus nanofabric is

fabricated via incorporating gelatin-functionalized conductive nanofabric as a polysulfide-blocking layer, and gelatin nanofabric as a low-resistance ion-flux regulator into an asymmetric configuration. The conductive nanofabric functionalized by gelatin shows good polysulfide-trapping ability due to gelatin's strong interaction with polysulfides; the gelatin nanofabric shows exceptional wettability, high ionic conductivity and high Li-ion transference number (0.73), therefore enabling to homogenize Li ion flux and stabilize Li metal. As a result, the Li/Li symmetrical cell with the gelatin nanofabric yields long cycle life over 1000 h with a fixed capacity of 0.5 mAh cm^{-2} . The Li-S cell with the Janus nanofabric shows excellent C-rate performance and stable cycling performance for 300 cycles at 0.5 A g^{-1} with a low capacity decay rate of 0.117% per cycle.

Results and discussion

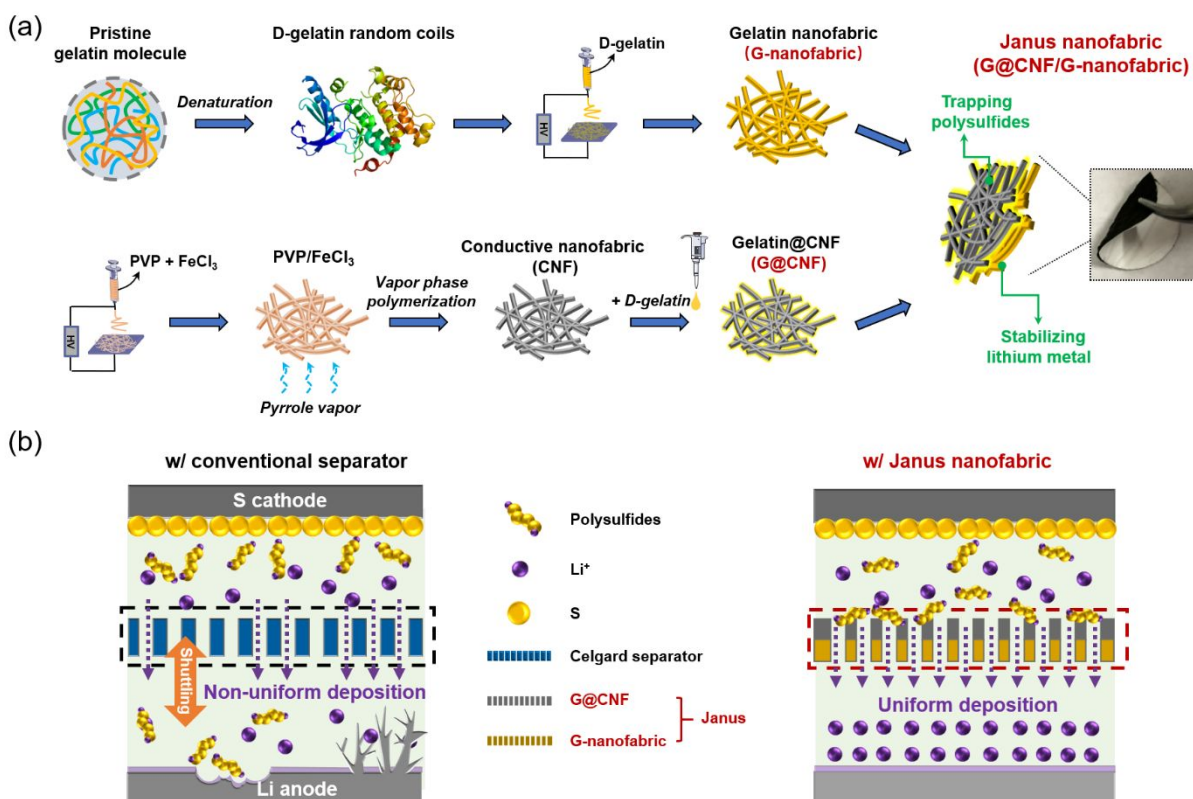


Figure 1. Fabrication of the protein-based Janus nanofabric and its effect on trapping polysulfides and stabilizing ion deposition. a) Schematic illustration of the fabrication process of the Janus nanofabric. The Janus nanofabric consists of an upper layer of gelatin-functionalized conductive nanofabric and a lower layer of gelatin nanofabric. (b) Schematic illustration of the contribution from conventional separator and Janus nanofabric to polysulfide diffusion and Li-ion deposition in Li-S batteries.

Figure 1a shows the schematic illustration for the fabrication process of the protein-based Janus nanofabric. The Janus nanofabric is composed of gelatin-coated conductive nanofabric for blocking the polysulfides and insulative gelatin nanofabric for guiding the ion deposition. The gelatin nanofabric (G-nanofabric) was fabricated via electrospinning of denatured gelatin solution where the pristine gelatin molecule was disrupted into random polypeptide coils with functional groups exposed. The conductive nanofabric (CNF) was derived from coating polypyrrole (Ppy) on polyvinylpyrrolidone (PVP) nanofibers via vapor-phase polymerization of pyrrole monomer⁴⁴. Denatured gelatin solution was then coated on the conductive nanofibers by drop casting to result in gelatin-functionalized CNF (G@CNF). More experimental details can be found in Experimental section. As shown in **Figure 1b**, Li-S batteries with a conventional separator suffer from the shuttling of polysulfides and uncontrollable growth of Li dendrites. The shuttling of polysulfides not only consumes the S active material but also corrodes the Li metal. Meanwhile, the formation of Li dendrites resulting from the inhomogeneous deposition of Li ions severely threatens the battery safety. By contrast, in an improved Li-S battery, the Janus nanofabric with the G@CNF toward S cathode and G-nanofabric toward Li anode can trap and convert the dissolved polysulfides to restrain the shuttle effect and protect the Li metal simultaneously. Specifically, the gelatin protein on the G@CNF layer can absorb polysulfides while the G-nanofabric layer can

regulate and homogenize the Li-ion flux and thus inhibit the growth of Li dendrites, leading to enhanced performance of Li-S batteries.

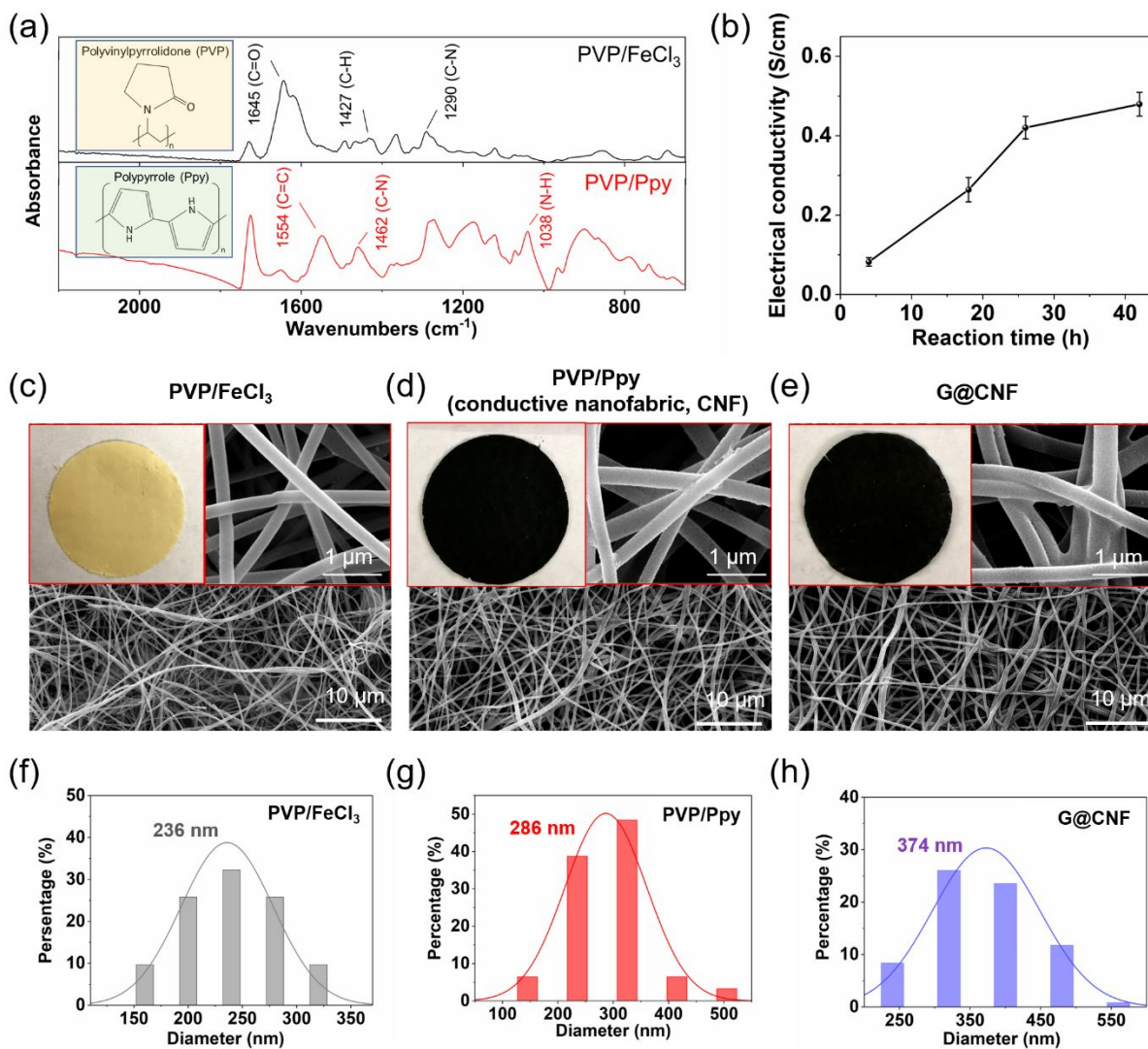


Figure 2. Morphological studies of gelatin-coated conductive nanofabric. a) FTIR spectra of PVP and PVP/Ppy nanofabrics. b) Electrical conductivity of PVP/Ppy nanofabric as a function of polymerization time. c-e) SEM images of c) PVP nanofabric, d) PVP/Ppy nanofabric (CNF) and e) G@CNF. f-h) Diameter distributions of f) PVP nanofabric, g) PVP/Ppy nanofabric and h) G@CNF.

The FTIR spectra of PVP nanofibers and the polymerized product, PVP/Ppy nanofibers, are shown in **Figure 2a**. For the PVP nanofibers, the absorption peak located at around 1645 cm^{-1} is ascribed to the stretching vibration of C=O, while the C-H bending and CH_2 wagging are observed at 1423 cm^{-1} and 1288 cm^{-1} , respectively. After polymerization, new peaks that are characteristics of polypyrrole appear, including the band at 1554 cm^{-1} corresponding to the ring stretching vibrations of the C=C bond, the band at 1462 cm^{-1} representing the C-N stretching and the N-H in plane deformation absorption at 1038 cm^{-1} . To endow the nanofabric with electrical conductivity to assure electrochemical conversion of trapped polysulfides, Ppy was polymerized on the PVP nanofiber surface, and the electrical conductivity varies with the amount of polymerized Ppy. As shown in **Figure 2b**, longer reaction time for vapor-phase polymerization leads to more Ppy generated and thus higher electrical conductivity. After reacted for 26 hours and 40 hours, the electrical conductivities of resulting nanofibers achieve 0.42 S cm^{-1} and 0.48 S cm^{-1} , respectively. Since the conductivity increasement of the PVP nanofibers after 26 hours is not significant, 26 hours was chosen for preparation of conductive nanofibers if it is not specifically noted.

The digital photos and SEM images of the nanofibers at different fabrication stages are shown in **Figure 2c-e**. As the morphologies of the nanofabric, i.e. fiber diameter and pore size, are critical contributors to the ability of trapping polysulfides, the concentration of the precursor solution for electrospinning was varied from 7 to 9 wt% to tune the fiber morphologies. **Figure S1** shows the diameter distributions of PVP nanofibers obtained from various concentrations of the precursor solutions. The fiber diameter significantly decreases with the solution concentration and 7 wt% yields the thinnest fiber diameter of 236 nm. Likewise, the pore size distribution of the resulting CNF shows the consistent tendency and 7 wt% generates the smallest average pore size of 864 nm in **Figure S2**. Because thinner nanofibers generate higher surface area and surface energy for

trapping polysulfides, 7 wt% precursor solution is used for fabricating the PVP nanofabric for the rest of the studies. As shown in **Figure 2c**, the PVP nanofabric is yellow-colored due to the presence of FeCl_3 and has smooth surface. After polymerization of pyrrole in **Figure 2d**, the nanofabric turns black (see the inset) and has rough surface. Meanwhile, the fiber diameter obviously increases from 236 nm to 286 nm (**Figure 2f, g**). These results indicate that Ppy layer was successfully formed on the fiber surface during polymerization process with a thickness of about 25 nm. Moreover, the photographs in **Figure S3** indicate that both PVP nanofabric and CNF have superior flexibility, which can sustain from severe mechanical deformations. For the G@CNF sample in **Figure 2e**, gelatin coating can be clearly observed on the fiber surface especially at the cross section, and the interconnected fibrous structure is still maintained. The average diameter of G@CNF is about 374 nm compared with CNF of 286 nm (**Figure 2h**), confirming the existence of gelatin coating on the CNF surface with a thickness of ~ 44 nm.

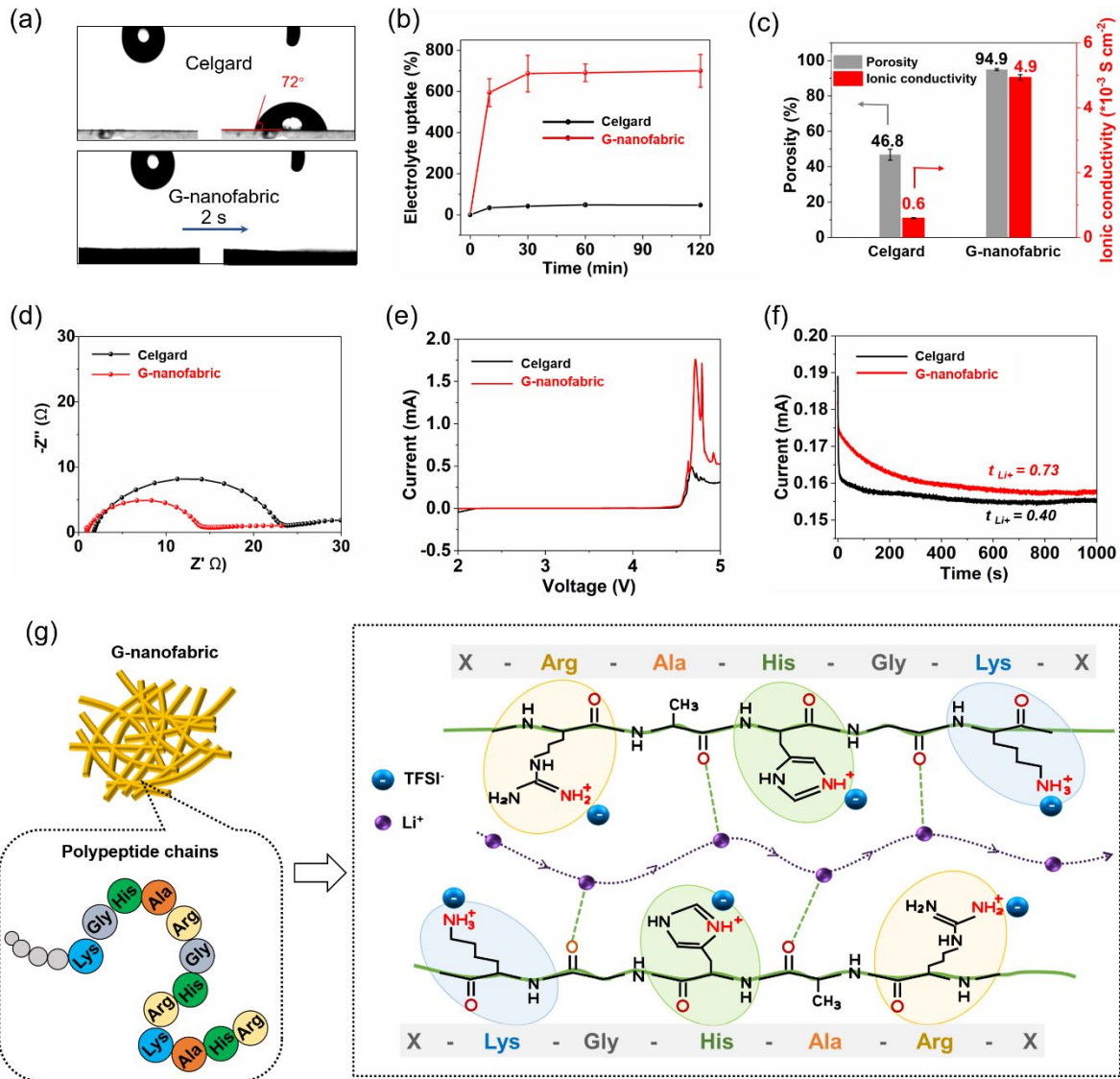


Figure 3. Electrochemical properties of G-nanofabric. a) Contact angles between liquid electrolyte droplets and G-nanofabric compared with Celgard® separator. b) Electrolyte uptake, and c) porosity and ionic conductivity of G-nanofabric and Celgard® separator. d) Nyquist plots showing the comparison of interfacial stability against Li metal in Li/separator/Li cells. e) Linear sweep voltammetry (LSV) curves of G-nanofabric and Celgard® separator in Li/separator/stainless steel cells at a scan rate of 0.1 mV/s. f) Current response of Li/separator/Li cells under steady state polarization. g) Schematic illustration of the possible ion-transport

situation for the G-nanofabric.

The G-nanofabric as the multifunctional insulating layer should obtain appropriate pore structure to feed liquid electrolytes for providing fast ion-conduction pathways. The SEM images of G-nanofabric can be found in **Figure S4**, which show that the average fiber diameter of G-nanofabric is ~ 538 nm. The affinity between G-nanofabric and electrolytes is characterized by contact angle measurement. The Celgard® separator shows a poor wettability to electrolytes with a large contact angle of 72° in equilibrium state. However, the wettability of G-nanofabric is excellent and the electrolyte droplet immediately infiltrates the nanofabric within 2 s (**Figure 3a**). Moreover, the electrolyte droplet can also quickly penetrate G@CNF (**Figure S5**) resulting in a contact angle of 0° ; thus, combining the G-nanofabric and G@CNF into a Janus nanofabric, superior affinity with liquid electrolytes can be achieved. Besides, the electrolyte uptake of G-nanofabric is much higher than that of Celgard® separator. As shown in **Figure 3b**, the G-nanofabric shows an extremely high electrolyte uptake of about 700% compared with that of Celgard® separator (ca. 48%). In addition, G-nanofabric shows a high porosity of 94.9% than that of Celgard® separator (46.8%) (**Figure 3c**). To be noted, the conductive G@CNF layer also shows a high porosity of 79.4%. The high wettability, porosity and electrolyte uptake of G-nanofabric benefits from the good fibrous structure and the hydrophilic groups from gelatin (e.g. amine and carboxyl groups. See the FTIR in **Figure S6**), which improves the ion-conduction ability of the G-nanofabric. As shown in **Figure 3c**, the ionic conductivity of G-nanofabric is $4.9 \times 10^{-3} \text{ S cm}^{-1}$, which is about one order of magnitude higher than that of Celgard® separator ($0.6 \times 10^{-3} \text{ S cm}^{-1}$).

Figure 3d shows the initial interface impedance spectra of Li/separator/Li cells with G-nanofabric or Celgard® separator. The initial charge-transfer resistance can be obtained from the diameter of the semicircle on the real axis. The resistances for G-nanofabric and Celgard® separator are 12.7

Ω and 21.8Ω , respectively, indicating that G-nanofabric shows better interfacial stability against Li metal. The electrochemical stability is characterized from the system of linear sweep voltammogram (LSV) using a cell of Li/separator/stainless steel (SS). In **Figure 3e**, the LSV curves of gelatin and Celgard® are both smooth and steady up to 4.5 V. The abrupt current growth above 4.5 V is due to the decomposition of liquid electrolytes⁴⁸. This result indicates that G-nanofabric is electrochemically stable up to 4.5 V and can satisfy the potential window for operation of Li-S batteries.

In addition, the Li-ion transference number (t_{Li^+}) is estimated using the Li/separator/Li cell via combination measurements of AC impedance and DC polarization, which was originally proposed by Evans and Vincent⁴⁹, and later refined by Abraham and Jiang⁵⁰. **Figure 3f** shows the initial and steady current flowing through the cell during polarization under an applied voltage of 10 mV. The AC impedance before and after polarization can be found in **Figure S7**. The G-nanofabric exhibits a much higher t_{Li^+} of 0.73 than that of Celgard® separator (0.40). The lone-pair electrons of the nitrogen heteroatoms in proteins can coordinate with Li^+ ions.⁵¹ The complex Li^+ ions will dissociate from their complexation sites and conjugate with new sites, leading to a motion of Li^+ ions^{24, 52}. In specific, from our previous studies³⁸, the negatively charged amino acids (Arg. His. and Lys.) that attract anions (TFSI⁻) act as coordination sites, while the backbone oxygens in the gelatin polypeptide chains have good affinity to Li^+ , enabling the fast hopping of Li^+ ions between these oxygen atoms, as depicted in **Figure 3g**.

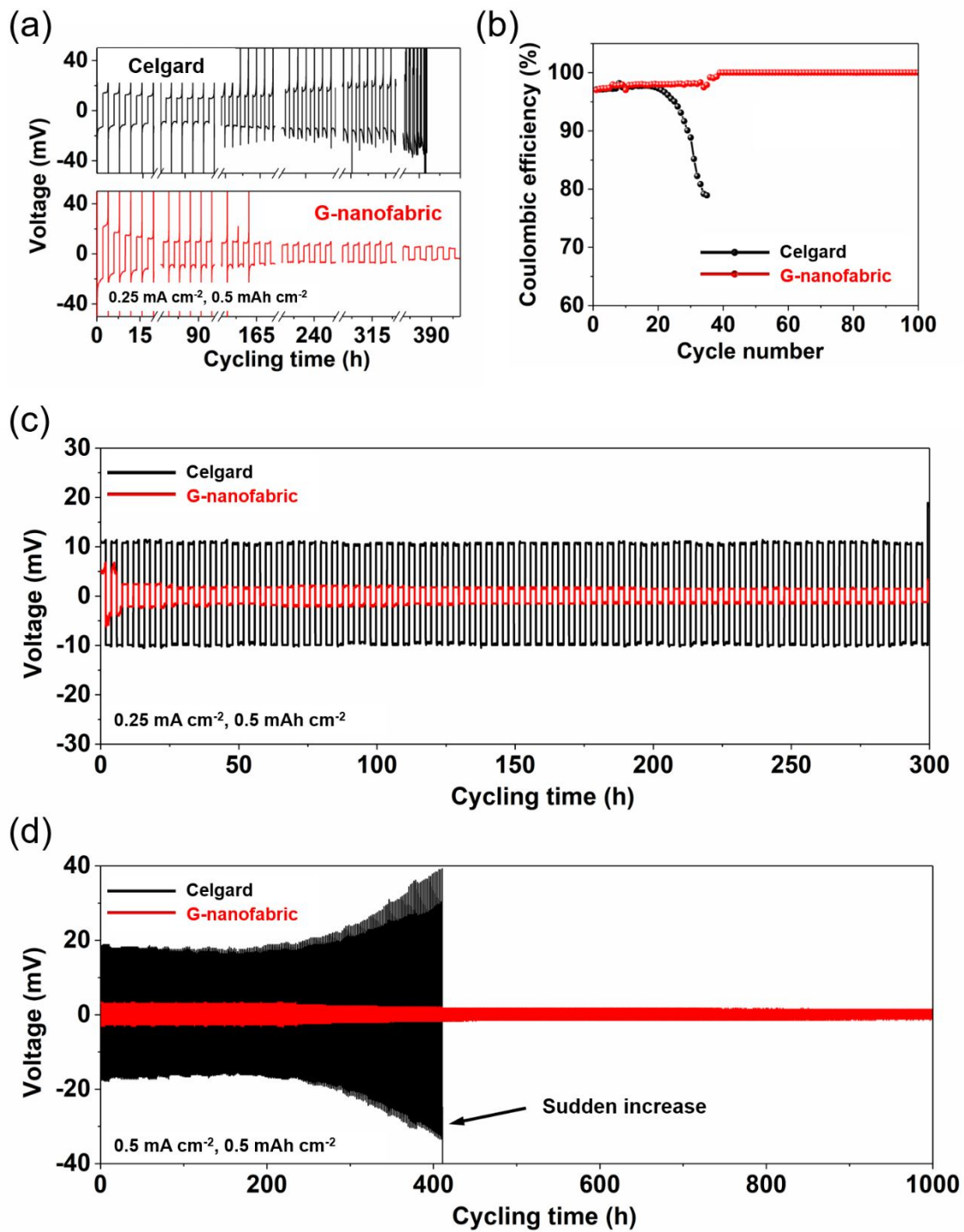


Figure 4. Li stripping/plating behaviors of gelatin nanofabric. a) Voltage profiles of Li/Cu cells during Li stripping/plating cycling at a current density of 0.25 mA cm^{-2} . b) Coulombic efficiency of the stripping/plating process on Cu electrode with different separators. c, d) Voltage

profiles of Li/Li symmetric cells at a current density of c) 0.25 mA cm^{-2} and d) 0.5 mA cm^{-2} .

Interestingly, it is found that the G-nanofabric is effective in stabilizing Li metal. The Li plating/stripping behavior was first analyzed in Li/Cu cells in which Li was stripped from Li anode and plated onto a Cu electrode during the discharge process and the process returned during charging. The contrast in the potential profiles using different separators is shown in **Figure 4a**. The complete voltage profiles of the whole 400 h cycling can be found in **Figure S8**. It can be seen that the cell with Celgard® separator shows gradually increased overpotential upon cycling, demonstrating high resistance for Li nucleation and unstable SEI formation⁵³. The unstable SEI results in continuous consumption of Li ions and electrolytes, and eventually failure of the cell after about 380 h. On the contrary, the gelatin cell shows a high overpotential in first three cycles and then the potential hysteresis is decreased and stabilized gradually. This indicates that the deposited Li can be smoothly stripped and uniform and stable SEI can be formed. The Coulombic efficiency of Li plating/stripping process is shown in **Figure 4b**. Gelatin cell shows a high efficiency of about 98.0% in the first 40 cycles, which increases to 99.9% after stabilization. This indicates that the G-nanofabric is able to stabilize Li metal by forming thin and stable SEI and Li can be stably and almost completely removed from Cu electrode in stripping process. In contrast, the cell with Celgard® separator exhibits an inferior performance after 20 cycles, with a rapid drop in Coulombic efficiency, which results from the formation of Li dendrites and loss of the activated Li metal⁵⁴. The unstable SEI in the Celgard® cell fosters the growth of Li dendrite and induces the isolation of Li particles, causing an irreversible consumption of Li. At a higher current density of 0.5 mA cm^{-2} , the Li/Cu cell with G-nanofabric maintains the low polarization and long cycle life of more than 600 h (**Figure S9**), confirming that the G-nanofabric is beneficial to stabilize Li metal.

Moreover, Li stripping/plating behavior was further studied in Li/Li symmetric cells as shown in **Figure 4c, d**. The polarization of gelatin cell (~ 3 mV) is significantly lower than that of the Celgard® cell (~ 10.5 mV) during 300 h of cycling, which implies that the G-nanofabric enables fast and stable deposition of Li^+ ions and help the nucleation of Li. At a higher current density of 0.5 mA cm^{-2} (**Figure 4d**), Celgard® cell exhibits rapidly increasing overpotential during cycling and shorts at about 400 h due to the penetration of Li dendrites. The poor performance is due to the unstable deposition of Li^+ ions, which further drives the growth of Li dendrites, and eventually piercing of Li dendrites through the separator. By contrast, gelatin cell presents an ultra-long lifespan of more than 1000 h with a low and stable overpotential (~ 2.1 mV). All these results verify that the G-nanofabric can effectively stabilize the deposition of Li^+ ions, leading to significant improvement in Li stripping/plating performance.

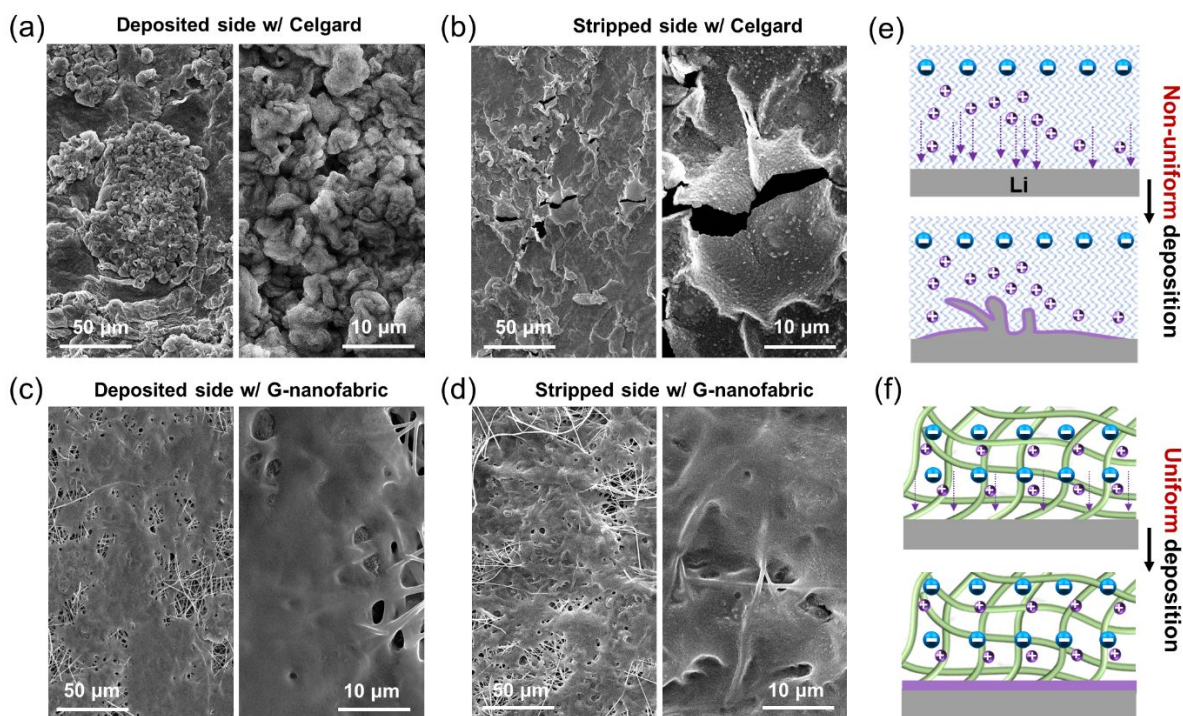


Figure 5. Morphological studies of post-mortem Li metals. a-d) Morphology of Li metals after 26 cycles of plating or stripping of Li in Li/Li symmetric cells with a, b) Celgard® and c, d) G-nanofabric. e, f) Schematic illustration of the Li deposition processes with Celgard® or gelatin separators.

To reveal how the G-nanofabric contributes to stabilizing the ion deposition, the morphologies of the post-mortem Li metals were investigated. The morphology of fresh Li metals can be found in **Figure S10**, showing that the surface is flat and smooth. **Figure 5a-d** shows the morphologies of Li metals after plating or stripping of Li in Li/Li symmetric cells. For the Li metal with Celgard® separator (**Figure 5a**), after depositing Li, considerable nodule-like Li appears resulting in uneven and rough surface, indicating unstable ion deposition and severe growth of Li dendrites. More seriously, in stripping process, the unstable SEI layer even cracks, which aggravates the interfacial instability and accelerates the generation of dead Li. The continuous forming/breaking of SEI layer

highly consumes Li and electrolytes and drives the growth of Li dendrites, which results in the increasing overpotential and finally short-circuit shown in **Figure 4d**. On the contrary, the Li metal with G-nanofabric exhibits significant morphology change. As shown in **Figure 5c**, for both deposited and stripped Li metals, smooth and homogeneous Li is embedded inside the nanofibers, which fills the opening space among the individual fibers and even forms film-like structure. The 3D fibrous structure lowers the local current densities and avoids the formation of “hot spots” by increasing the effective surface area⁵⁵, leading to stable and homogenous deposition of lithium ions. As a result, the growth of Li dendrites is suppressed, thus resulting in exceptional long-term Li plating/stripping performance with stable and low overpotential as discussed above in **Figure 4d**.

In addition to the advantages of the 3D fibrous structure of G-nanofabric in suppressing the dendritic Li growth, the unique electrochemical properties of G-nanofabric acts as additional benefits. As discussed in **Figure 3f**, the G-nanofabric exhibits a high Li-ion transference of 0.73, implying that anions can be largely anchored by the nanofabric. As is well known that, the “Space Charge Model”⁵⁶ attributes the growth of Li dendrites to the depletion of anions in the vicinity of the anode surface. Increasing the Li-ion transference number is believed to be a plausible way for delaying the Sand’s time (dendrite nucleation time) or stabilizing the electrodeposition.⁵⁷ Therefore, as depicted in **Figure 5e**, for the cell with Celgard® separator, the space charge region leads to inhomogeneous distribution of Li⁺ ions, resulting in preferential deposition of Li at relatively sharp tips of the protuberances, which is commonly known as the “tip effect”. The concentrated Li⁺ ion flux expedites the nucleation and growth of Li metal at some local points, which gradually evolves into Li dendrites²⁶. By contrast, the G-nanofabric with a high Li-ion transference number helps prevent the depletion of anions near the Li metal surface in Li-plating process. As illustrated in **Figure 5f**, the G-nanofabric plays two roles here in stabilizing the Li

metal: 1) the anions are highly immobilized by the nanofabric, helping stabilize the electric field and diminish the space charge region; 2) the G-nanofabric with surface polarity having good affinity with Li^+ ions, thus acting as a redistributor for Li^+ ion flux.²⁵ As a result, the Li^+ ion flux is homogenized over the entire Li-metal area during cycling and therefore Li-dendrite growth is suppressed⁵⁸. Finally, planar Li metals embedded inside the fiber matrix is formed as can be seen in **Figure 5c, d**. Due to the synergistic effect from the G-nanofabric, the cycle performance of Li/gelatin/Li cell is far superior than that of Li/Celgard®/Li cell.

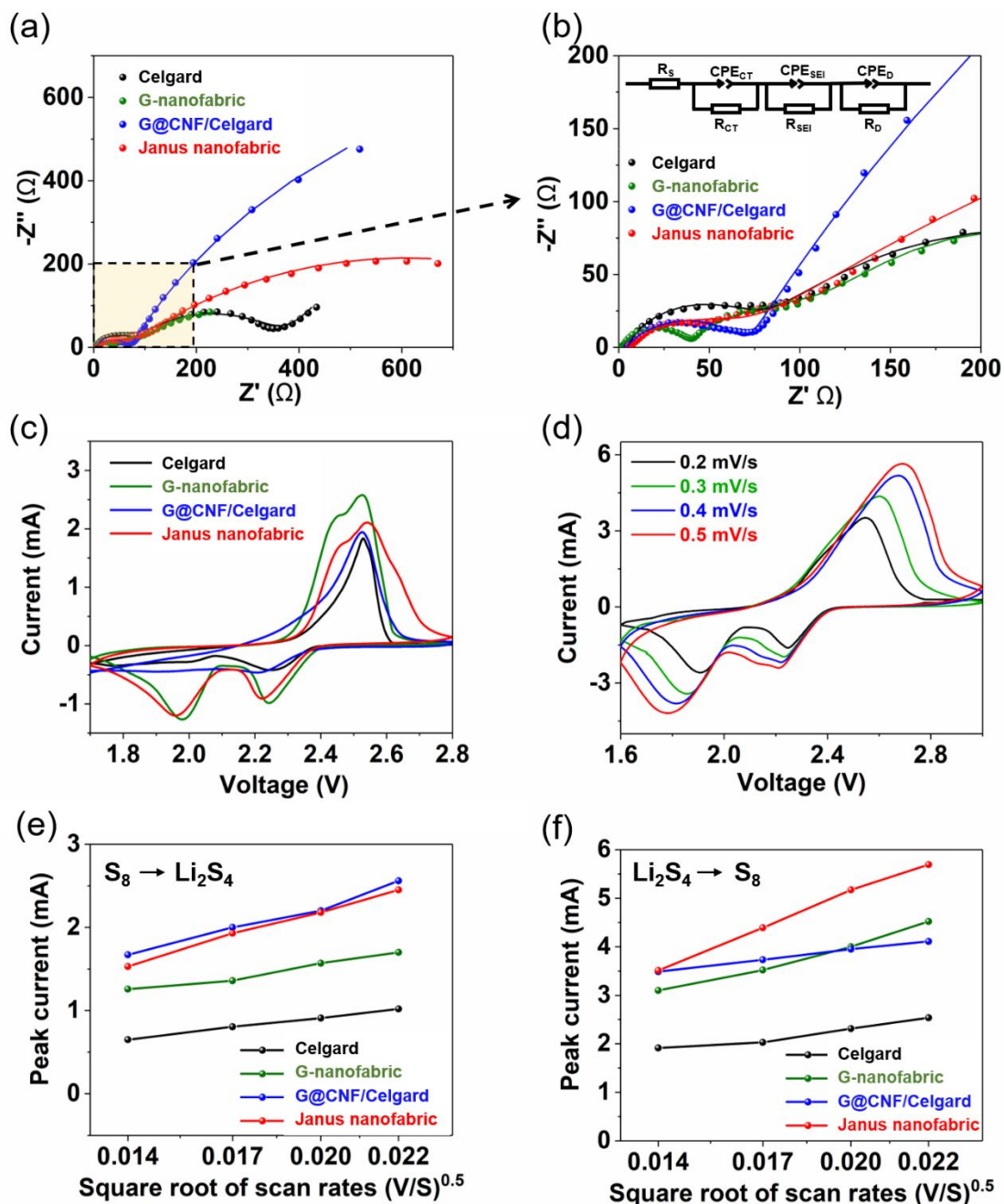


Figure 6. Electrochemical performance of Li-S batteries with Janus nanofabric compared with counterparts. a, b) Electrochemical impedance spectra of Li-S cells with different separators over a frequency range of 0.01-1 MHz. The solid lines indicate the fitting results. c) CV curves of Li-S cells with different separators at a scan rate of 0.1 mV s⁻¹. d) CV curves of Li-S cells with

Janus nanofabric at different scan rates. e, f) Plots of CV peak current of e) the cathodic reaction ($S_8 \rightarrow Li_2S_4$) and f) the anodic reaction ($Li_2S_4 \rightarrow S_8$) versus the square root of scan rates.

To understand the significant impact of the Janus nanofabric on Li-S cells, electrochemical impedance spectroscopy (EIS) was conducted on the fresh cells at discharged state. Typical EIS plots with equivalent circuit models are shown in **Figure 6a, b** and the electrochemical impedance parameters are summarized in **Table S1** (Supporting Information). The intercepts of the plots on the real axis at high frequency are related to the bulk resistance (R_b). For cells with G@CNF/Celgard® or G@CNF/G-nanofabric (Janus nanofabric), the Nyquist plots are composed of a single semicircle and an inclined line, which are corresponding to the charge-transfer process (a parallel connection of R_{CT} and CPE_{CT}) and a diffusion process (simulated by $R_D//CPE_D$)⁵⁹, respectively. As for cells with Celgard® separator or G-nanofabric, there are two sequential semicircles at the high-to-medium frequency region. Besides the one indicating the charge transfer process (at high frequency region), the another one at medium frequency region corresponds to interface impedance (a parallel connection of R_{SEI} and CPE_{SEI}) that indicates Li-ion diffusion resistance through the Li_2S/Li_2S_2 solid film.³¹ Firstly, regarding the Celgard® separator and G-nanofabric, the R_{CT} (36.8 Ω) of G-nanofabric is much smaller than that of Celgard® separator (67.8 Ω) mainly because of the high ionic conductivity of G-nanofabric. Secondly, compared with the cells without G@CNF interlayer, the R_{SEI} of G@CNF modified cells, i.e. the cells with G@CNF/Celgard® and Janus nanofabric, is negligible, which suggests that the G@CNF interlayer inhibits the diffusion of dissolved polysulfides from S cathode side to Li anode; thus almost no Li_2S/Li_2S_2 solid film forms after first discharging. To be more specific, the cell with Janus nanofabric shows much smaller R_{CT} of 60.9 Ω compared with 66.6 Ω for the G@CNF/Celgard® cell, which benefits from the high ionic conductivity of G-nanofabric. Interestingly, the R_{SEI} (83.1

Ω) of the cell with only G-nanofabric is even smaller than half of that of Celgard® (194.9 Ω) cell, which is ascribed to the strong capability of gelatin for trapping polysulfides, although the large pores of the G-nanofabric still allows some diffusion of polysulfides. The EIS results reveal that 1) G-nanofabric has low charge-transfer resistance and some effect in trapping polysulfides, making it a low-resistance “secondary guard” for blocking the diffusion of polysulfides to Li anode side; 2) G@CNF is very effective in trapping polysulfides. Therefore, incorporation of G@CNF and G-nanofabric into a Janus configuration is beneficial to attain a low-resistance separator for trapping polysulfides and assuring fast redox reaction.

Cyclic voltammetry (CV) was performed to study the reaction kinetics of Li-S batteries with different separators. As shown in **Figure 6c**, in cathodic scan the peak at around 2.25 V corresponding to the reduction of S_8 into high-order lithium polysulfides (Li_2S_x , $4 \leq x \leq 8$) can be observed in all cells. It is worth noting that the cells with gelatin or Janus nanofabrics exhibit much dominant peaks and higher peak currents at 1.95 V compared with the cells with Celgard® separators, suggesting that the G-nanofabric enables a fast reduction of soluble lithium polysulfides to insoluble lower-order lithium sulfides (Li_2S_2 or Li_2S). In the oxidation process, one merged peak can be observed in all cells, which suggests that lithium sulfides (Li_2S_2/Li_2S) are converted to soluble lithium polysulfides (Li_2S_x , $4 \leq x \leq 8$) and then finally to S_8 . It is found that the cells with gelatin and Janus nanofabrics display two well-defined redox peaks with high peak currents, indicating less polarization and a rapid conversion kinetics.[15]

In order to explore the Li-ion diffusion properties for different separators, CV measurements under different scanning rates ranging from 0.2 to 0.5 $mV s^{-1}$ were performed. **Figure 6d** shows the CV curves of the cell with Janus nanofabric at varying scan rates, which demonstrates that the peak current and polarization increases with the scan rate. The current contributed by the redox

processes in the bulk part of separator materials is generated by the directed diffusion of charge carriers, and it is linearly proportional to the square root of the scan rate.⁶⁰ Hence, Li-ion diffusion properties can be estimated according to the classical Randles Sevcik equation⁶¹ and the linear relationship between peak currents and square root of scan rates can be seen in **Figure 6e, f**. The slopes of the curves are positively correlated to the corresponding Li-ion diffusion coefficient. Since the binding of $\text{Li}_2\text{S}/\text{Li}_2\text{S}_2$ with the separator materials is mainly dependent on the two Li atoms, the Li ion diffusion can also indicate the diffusivity of sulfides species on the surface of the separators.⁶² During the discharging process in **Figure 6e**, the Janus nanofabric has the highest slope or Li-ion diffusion coefficient followed by G@CNF/Celgard®, indicating that the G@CNF layer helps trap and then convert the polysulfides to $\text{Li}_2\text{S}/\text{Li}_2\text{S}_2$, which reduces the viscosity of the electrolyte and prevents the deposition of insulating S-species on electrodes. Meanwhile, the G-nanofabric of the Janus nanofabric greatly benefits the diffusion of Li^+ ions due to its high ionic conductivity. In charging process (**Figure 6f**), the gelatin-containing separators outperform the two groups of cells with Celgard® separators, and the Janus nanofabric shows the highest Li-ion diffusion coefficient. This is possibly because the reduction of Li^+ to Li metal becomes a dominant factor and Li^+ ions diffuse faster with G-nanofabric.

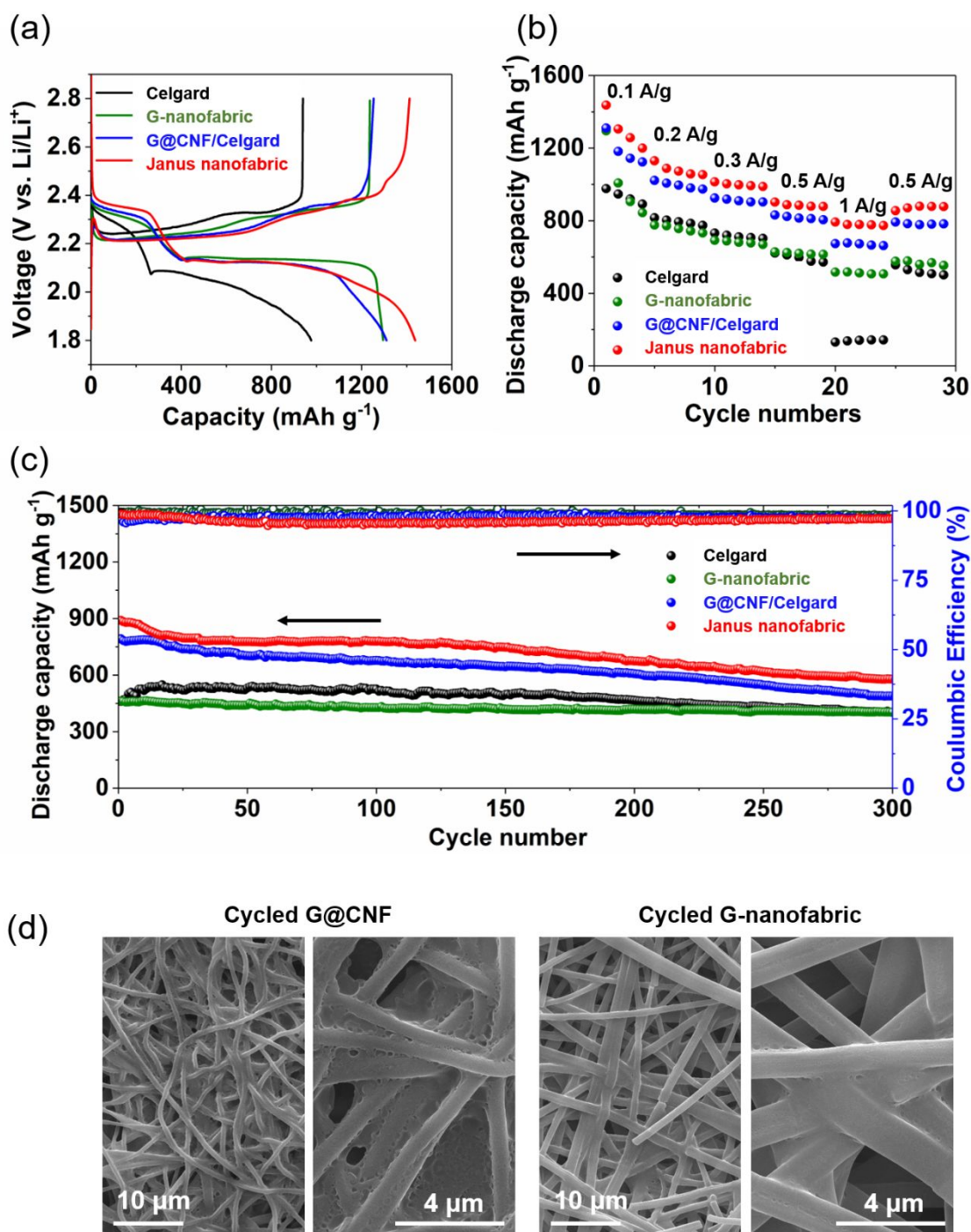


Figure 7. Charge-discharge performance of Li-S batteries with Janus nanofabric compared with counterparts. a) Charge-discharge profiles of Li-S cells with different separators at 0.1 mA g^{-1} . b) Rate performances of Li-S cells. c) Cycling performance of Li-S cells at 0.5 A g^{-1} . d, e)

SEM images of the two layers of Janus nanofabric: d) G@CNF and e) G-nanofabric, disassembled from cycled Li-S cells at discharged state.

To further reveal the advantages of the Janus nanofabric, electrochemical performances of Li-S batteries with different separators are compared. The untreated conductive nanofabric interlayer with smaller diameter delivers higher discharge capacity due to higher surface area, as shown in **Figure S11**. Taking a closer look, one can find that the capacity difference between the samples of 7 wt% and 9 wt% decreases with current density, which possibly results from the pore size distribution. As discussed in **Figure S2**, CNF interlayer obtained from 9 wt% solution has large pore size thus shows less resistance for lithium ion transport. Therefore, the inferiority of 9 wt% CNF is reduced at a high current density of 1 A g⁻¹. It has been reported that gelatin protein has strong interaction with polysulfides due to the oxygen atoms in backbone⁶³, which can be reflected from the cycle performance comparison in **Figure S12** that G@CNF shows higher capacity and slower decay than that of CNF. As shown in **Figure 7a**, the cell with Janus nanofabric shows the highest initial discharge capacity (1438 mAh g⁻¹) followed by G@CNF/Celgard® (1310 mAh g⁻¹), compared with conventional G-nanofabric (1295 mAh g⁻¹), Celgard® separator (978 mAh g⁻¹). Specifically, the Janus nanofabric leads to the greatest utilization of sulfur active materials of as high as 85.9%. These results suggest that the G@CNF layer effectively suppresses the diffusion of polysulfides and the loss of sulfur active materials. Meanwhile, in comparison of Celgard® separator, G-nanofabric shows some ability to trap polysulfides as evidenced by the higher capacity than that of Celgard® separator. The voltage profiles are also compared at a current density of 0.3 A g⁻¹ (**Figure S13**), in which Janus nanofabric shows advantages in high capacity and G-nanofabric helps reduce the polarization. **Figure 7b** plots the specific discharge capacities versus different current densities. The cell with Celgard® separator shows the poorest rate

performance that the discharge capacity is as low as 138.9 mAh g⁻¹ at a current density of 1 A g⁻¹. Replacing the Celgard® separator with G-nanofabric, though the capacities at low current densities are similar, the capacity at 1 A g⁻¹ is dramatically improved (up to 512.0 mAh g⁻¹), benefiting from the low charge-transfer resistance (**Figure 6a, b**). Inserting a G@CNF layer improves the capacity because of the strong polysulfide-trapping ability and the high electrical conductivity. Besides, the 3D conductive skeleton of the G@CNF layer provides large surface area for electronic contacts with captured polysulfides and more channels for ionic transfer^{64, 65}. Therefore, the G@CNF/Celgard® and Janus nanofabric yield much higher capacities than that of only Celgard® separator or G-nanofabric at all current density ranges. Specifically, the Janus nanofabric delivers the highest discharge capacities of 1266, 1040, 970, 883 and 780 mAh g⁻¹ at the current densities of 0.1, 0.2, 0.3, 0.5 and 1 A g⁻¹, respectively. When the current density is changed back to 0.5 A g⁻¹, the capacity recovers to 872 mAh g⁻¹ with a retention of 98.8%. The exceptional rate performance of the Janus nanofabric is the combined result of low-resistance of G-nanofabric and effective capture-convention of polysulfides by G@CNF, which leads to fast ion-transport, reduced loss of sulfur species, and smooth polysulfide-conversion kinetics. The diffusion experiment results in **Figure S14** verify the polysulfide-trapping capability of the Janus separator. It apparently shows that the Janus separator effectively suppressed the diffusion of polysulfides in the course of the 24 h-diffusion test, as the much lighter color of the electrolyte solution at the bottom indicates a mitigated contamination from the polysulfide-diffusion compared with the Celgard® separator.

The cycle performance of different separators is compared in **Figure 7c**. The pristine Celgard® cell yields an initial discharge capacity of 525 mAh g⁻¹ after activation and the capacity decays to 399 mAh g⁻¹ after 300 cycles, due to a substantial loss of sulfur active materials and the severe

shuttle effect. With the introduction of G@CNF layer, the G@CNF/Celgard® cell exhibits improved discharge capacity with an initial discharge capacity of 792 mAh g⁻¹ and a decay rate of 0.128% per cycle. Compared with Celgard® separator, G-nanofabric shows extremely stable cycling capacity that after 300 cycles the capacity retention is as high as 87.4% of the initial capacity. However, the overall capacity is lower than that of the Celgard® separator. As shown in **Figure S15**, the G-nanofabric disassembled from cycled batteries shows severe accumulation of S-species filling the pores due to strong adsorption of polysulfides by gelatin, which blocks the ion-conduction pathways. This results in the low capacity of the cell with G-nanofabric. More significantly, the Janus nanofabric cell presents the highest capacities throughout the tested cycles. The initial capacity and retention capacity after 300 cycles are 890 mAh g⁻¹ and 577 mAh g⁻¹, respectively. The results clearly indicate that Janus nanofabric effectively inhibits the shuttle effect and ensures sufficient redox reactions. Despite that the Coulombic efficiency of Janus separator is relatively low, the effectiveness in suppressing the shuttle effect can be justified due to two reasons. First, the capacities of the cells with Janus separator and G@CNF/Celgard® are much higher than that of the cells without G@CNF, which indicates that polysulfides are massively blocked and re-utilized by G@CNF. The lower Coulombic efficiencies of these two cells are mainly led by the mitigated diffusion of polysulfides gradually occurring over cycling, in contrast to the cells without G@CNF that sulfur promptly consumes and becomes scarified species, thus showing higher Coulombic efficiencies. Second, in comparison with the pristine Celgard® separator, the cell with G@CNF/Celgard® separator shows a comparative Coulombic efficiency, while the Janus separator shows a slightly inferior efficiency. This suggests that G@CNF is effective in suppressing the shuttle effect, but the large pores (average pore size: ca. 1.65 μm) of G-nanofabric (see **Figure S4c**) may result in a loss of sulfur species. By refining the morphologies of G-

nanofabric, the performance of the Janus separator is anticipated to be further improved.

The SEM images of two layers, G@CNF and G-nanofabric, of cycled Janus nanofabrics are shown in **Figure 7d**. Compared with fresh G@CNF in **Figure 2e**, the cycled G@CNF are covered by S-species resulting in formation of film-like structure, which confirms the ability of G@CNF to capture polysulfides. By contrast, the cycled G-nanofabric still maintains its fibrous structure, although some S-species accumulates along the fibers. This suggests that polysulfides are greatly adsorbed by the G@CNF layer. Thus, only few polysulfides diffuse to the G-nanofabric layer, which can be captured by the G-nanofabric being as the “secondary guard”. The foremost advantage of Janus configuration is the capabilities of suppressing both the shuttle effect and dendrite growth without creating redundant layers. However, the thickness of the Janus separator is $\sim 35 \mu\text{m}$, which needs to be further reduced to meet the practical applications. With processing technologies being refined and structure control of the nanofabrics being optimized, a further reduction of thickness and mass is expected.

Conclusion

In summary, we report a protein-based, low-resistance Janus nanofabric capable of capturing polysulfides and stabilizing lithium metal simultaneously. The Janus nanofabric is fabricated via incorporation of gelatin-functionalized conductive nanofabric as a polysulfide-trapping layer, and gelatin nanofabric as a low-resistance ion-regulating layer, into an asymmetric configuration. The conductive nanofabric boosted by gelatin-coating demonstrates good ability to trap polysulfides due to gelatin's chemisorption of polysulfides. The gelatin nanofabric shows excellent electrolyte uptake (700 %), high ionic conductivity ($4.9 \times 10^{-3} \text{ S cm}^{-1}$) and high Li-ion transference number (0.73), making it effective in stabilizing ion deposition. As a result, the symmetric Li/Li cells with gelatin nanofabric yield ultra-long cycle life over 1000 h and stable cycling performance.

Benefiting from the synergistic effect from the two functional layers, the resulting Janus nanofabric demonstrates low ion-transport resistance and excellent capabilities for both trapping polysulfides and suppressing dendritic Li growth. Adding the Janus nanofabric in Li-S batteries, the rate performance, capacity and cycling stability are significantly enhanced (e.g. initial discharge capacity of 890 mAh g⁻¹ with a decay rate of 0.117% up to 300 cycles at 0.5 A g⁻¹). This work provides an instructive and flexible strategy for development of multi-functional separators via combining constituents with rationally designed properties for high-power battery systems.

Acknowledgements

This work was supported by NSF CBET 1929236. Ms. Min Chen was sponsored by the China Scholarship Council for her visit at Washington State University. The authors would like to gratefully acknowledge the support on microscopy characterizations from the Franceschi Microscopy & Imaging Center at Washington State University.

References

1. A. Borenstein, O. Hanna, R. Attias, S. Luski, T. Brousse and D. Aurbach, *J. Mater. Chem. A*, 2017, **5**, 12653-12672.
2. M. Liu, B. Li, H. Zhou, C. Chen, Y. Liu and T. Liu, *Chem. Commun.*, 2017, **53**, 2810-2813.
3. H. Lee, M. Yanilmaz, O. Toprakci, K. Fu and X. W. Zhang, *Energy Environ. Sci.*, 2014, **7**, 3857-3886.
4. X.-C. Zhao, P. Yang, L.-J. Yang, Y. Cheng, H.-Y. Chen, H. Liu, G. Wang, V. Murugadoss, S. Angaiah and Z. Guo, *ES Materials & Manufacturing*, 2018, **1**, 67-71.
5. X. Fu and W. H. Zhong, *Adv. Energy Mater.*, 2019, **9**, 1901774.
6. H. Yuan, J. Q. Huang, H. J. Peng, M. M. Titirici, R. Xiang, R. Chen, Q. Liu and Q. Zhang, *Adv. Energy Mater.*, 2018, **8**, 1802107.
7. L. Zhang, Y. Wang, Z. Niu and J. Chen, *Carbon*, 2019, **141**, 400-416.
8. Q. Qi, X. Lv, W. Lv and Q.-H. Yang, *J. Energy Chem.*, 2019, **39**, 88-100.
9. W. Li, Q. Zhang, G. Zheng, Z. W. Seh, H. Yao and Y. Cui, *Nano Lett.*, 2013, **13**, 5534-5540.
10. G. Hu, C. Xu, Z. Sun, S. Wang, H. M. Cheng, F. Li and W. Ren, *Adv. Mater.*, 2016, **28**, 1603-1609.
11. S. H. Chung, C. H. Chang and A. Manthiram, *Energy Environ. Sci.*, 2016, **9**, 3188-3200.
12. M. Liu, Q. Meng, Z. Yang, X. Zhao and T. Liu, *Chem. Commun.*, 2018, **54**, 5090-5093.
13. M. Liu, Y. Liu, Y. Yan, F. Wang, J. Liu and T. Liu, *Chem. Commun.*, 2017, **53**, 9097-9100.
14. Y. Liu, Y. Yan, K. Li, Y. Yu, Q. Wang and M. Liu, *Chem. Commun.*, 2019, **55**, 1084-1087.
15. M. Liu, Z. Yang, H. Sun, C. Lai, X. Zhao, H. Peng and T. Liu, *Nano Research*, 2016, **9**, 3735-3746.
16. X. Liang, C. Hart, Q. Pang, A. Garsuch, T. Weiss and L. F. Nazar, *Nat. Commun.*, 2015, **6**, 5682.
17. Z. Z. Yang, H. Y. Wang, L. Lun, W. Cheng, X. B. Zhong, J. G. Wang and Q. C. Jiang, *Scientific Reports*, 2016, **6**,

- 22990.
18. J. Zheng, X. Fan, G. Ji, H. Wang, S. Hou, K. C. DeMella, S. R. Raghavan, J. Wang, K. Xu and C. Wang, *Nano energy*, 2018, **50**, 431-440.
 19. Y. Lu, X. Huang, Z. Song, K. Rui, Q. Wang, S. Gu, J. Yang, T. Xiu, M. E. Badding and Z. Wen, *Energy Storage Materials*, 2018, **15**, 282-290.
 20. Y. Jeong, J. Kim, S. Kwon, J. Oh, J. Park, Y. Jung, S. Lee, S. Yang and C. Park, *J. Mater. Chem. A*, 2017, **5**, 23909-23918.
 21. J. Qian, B. D. Adams, J. Zheng, W. Xu, W. A. Henderson, J. Wang, M. E. Bowden, S. Xu, J. Hu and J. G. Zhang, *Adv. Funct. Mater.*, 2016, **26**, 7094-7102.
 22. W. Li, H. Yao, K. Yan, G. Zheng, Z. Liang, Y.-M. Chiang and Y. Cui, *Nat. Commun.*, 2015, **6**, 7436.
 23. N. W. Li, Y. X. Yin, C. P. Yang and Y. G. Guo, *Adv. Mater.*, 2016, **28**, 1853-1858.
 24. Y. X. Tang, J. Y. Deng, W. L. Li, O. I. Malyi, Y. Y. Zhang, X. R. Zhou, S. W. Pan, J. Q. Wei, Y. R. Cai, Z. Chen and X. D. Chen, *Adv. Mater.*, 2017, **29**, 1701828.
 25. Z. Liang, G. Zheng, C. Liu, N. Liu, W. Li, K. Yan, H. Yao, P.-C. Hsu, S. Chu and Y. Cui, *Nano Lett.*, 2015, **15**, 2910-2916.
 26. X. B. Cheng, T. Z. Hou, R. Zhang, H. J. Peng, C. Z. Zhao, J. Q. Huang and Q. Zhang, *Adv. Mater.*, 2016, **28**, 2888-2895.
 27. J. Xiao, *Science*, 2019, **366**, 426-427.
 28. D. Lin, Y. Liu and Y. Cui, *Nat. Nanotechnol.*, 2017, **12**, 194.
 29. Y. C. Jeong, J. H. Kim, S. Nam, R. P. Chong and S. J. Yang, *Adv. Funct. Mater.*, 2018, **28**, 1707411.
 30. X. Fu, Y. Wang, L. Scudiero and W.-H. Zhong, *Energy Storage Materials*, 2018, **15**, 447-457.
 31. W. Kong, L. Yan, Y. Luo, D. Wang, K. Jiang, Q. Li, S. Fan and J. Wang, *Adv. Funct. Mater.*, 2017, **27**, 1606663.
 32. J.-L. Yang, S.-X. Zhao, Y.-M. Lu, X.-T. Zeng, W. Lv and G.-Z. Cao, *Nano Energy*, 2020, **68**, 104356.
 33. Y. Zang, F. Pei, J. Huang, Z. Fu, G. Xu and X. Fang, *Adv. Energy Mater.*, 2018, **8**, 1802052.
 34. S. Bai, X. Liu, K. Zhu, S. Wu and H. Zhou, *Nature Energy*, 2016, **1**, 16094.
 35. S. Tu, X. Chen, X. Zhao, M. Cheng, P. Xiong, Y. He, Q. Zhang and Y. Xu, *Adv. Mater.*, 2018, **30**, 1804581.
 36. H. M. Kim, H.-H. Sun, I. Belharouak, A. Manthiram and Y.-K. Sun, *ACS Energy Lett.*, 2016, **1**, 136-141.
 37. M. Chen, X. Fu, N. D. Taylor, Z. Chen and W.-H. Zhong, *ACS Sustainable Chem. Eng.*, 2019, **7**, 15267-15277.
 38. X. Fu, L. Scudiero and W.-H. Zhong, *J. Mater. Chem. A*, 2019, **7**, 1835-1848.
 39. M. Chen, C. Li, X. Fu, W. Wei, X. Fan, A. Hattori, Z. Chen, J. Liu and W.-H. Zhong, *Adv. Energy Mater.*, 2020, **10**, 1903642.
 40. W.-K. Shin, A. G. Kannan and D.-W. Kim, *ACS Appl. Mat. Interfaces* 2015, **7**, 23700-23707.
 41. W. Luo, L. Zhou, K. Fu, Z. Yang, J. Wan, M. Manno, Y. Yao, H. Zhu, B. Yang and L. Hu, *Nano Lett.*, 2015, **15**, 6149-6154.
 42. Y. Guan, A. Wang, S. Liu, Q. Li, W. Wang and Y. Huang, *J. Alloys Compd.*, 2018, **765**, 544-550.
 43. Y. Ye, L. Wang, L. Guan, F. Wu, J. Qian, T. Zhao, X. Zhang, Y. Xing, J. Shi and L. Li, *Energy Storage Materials*, 2017, **9**, 126-133.
 44. Y. Li, W. Wang, X. Liu, E. Mao, M. Wang, G. Li, L. Fu, Z. Li, A. Y. S. Eng, Z. W. Seh and Y. Sun, *Energy Storage Materials*, 2019, **23**, 261-268.
 45. K. Xie, K. Yuan, K. Zhang, C. Shen, W. Lv, X. Liu, J.-G. Wang and B. Wei, *ACS Appl. Mat. Interfaces* 2017, **9**, 4605-4613.
 46. L. Kong, X. Fu, X. Fan, Y. Wang, S. Qi, D. Wu, G. Tian and W.-H. Zhong, *Nanoscale*, 2019, **11**, 18090.
 47. Z. Li, Y. Han, J. Wei, W. Wang, T. Cao, S. Xu and Z. Xu, *ACS Appl. Mat. Interfaces* 2017, **9**, 44776-44781.
 48. C. Ding, X. Fu, H. Li, J. Yang, J. L. Lan, Y. Yu, W. H. Zhong and X. Yang, *Adv. Funct. Mater.*, 2019, **29**, 1904547.
 49. J. Evans, C. A. Vincent and P. G. Bruce, *Polymer*, 1987, **28**, 2324-2328.
 50. K. Abraham, Z. Jiang and B. Carroll, *Chem. Mater.*, 1997, **9**, 1978-1988.
 51. H. Wu, Q. Wu, F. Chu, J. Hu, Y. Cui, C. Yin and C. Li, *J. Power Sources* 2019, **419**, 72-81.
 52. J. Liu, Q. Zhang, T. Zhang, J. T. Li, L. Huang and S. G. Sun, *Adv. Funct. Mater.*, 2015, **25**, 3599-3605.
 53. X. Li, S. Guo, H. Deng, K. Jiang, Y. Qiao, M. Ishida and H. Zhou, *J. Mater. Chem. A*, 2018, **6**, 15517-15522.
 54. S. J. Zhang, Z. G. Gao, W. W. Wang, Y. Q. Lu, Y. P. Deng, J. H. You, J. T. Li, Y. Zhou, L. Huang and X. D. Zhou, *Small*, 2018, **14**, 1801054.
 55. C.-P. Yang, Y.-X. Yin, S.-F. Zhang, N.-W. Li and Y.-G. Guo, *Nat. Commun.*, 2015, **6**, 8058.
 56. N. Ohta, K. Takada, L. Zhang, R. Ma, M. Osada and T. Sasaki, *Adv. Mater.*, 2006, **18**, 2226-2229.

57. P. Bai, J. Li, F. R. Brushett and M. Z. Bazant, *Energy Environ. Sci.*, 2016, **9**, 3221-3229.
58. M. H. Ryou, D. J. Lee, J. N. Lee, Y. M. Lee, J. K. Park and J. W. Choi, *Adv. Energy Mater.*, 2012, **2**, 645-650.
59. N. A. Canas, K. Hirose, B. Pascucci, N. Wagner, K. A. Friedrich and R. Hiesgen, *Electrochim. Acta* 2013, **97**, 42-51.
60. X. Yang and A. L. Rogach, *Adv. Energy Mater.*, 2019, **9**, 1900747.
61. P. Li, L. Shao, P. Wang, X. Zheng, H. Yu, S. Qian, M. Shui, N. Long and J. Shu, *Electrochim. Acta* 2015, **180**, 120-128.
62. X. Tao, J. Wang, C. Liu, H. Wang, H. Yao, G. Zheng, Z. W. Seh, Q. Cai, W. Li and G. Zhou, *Nat. Commun.*, 2016, **7**, 11203.
63. X. Fu, C. Li, Y. Wang, L. Scudiero, J. Liu and W. H. Zhong, *J. Phys. Chem. Lett.*, 2018, **9**, 2450-2459.
64. M. Liu, P. Zhang, Z. Qu, Y. Yan, C. Lai, T. Liu and S. Zhang, *Nat. Commun.*, 2019, **10**, 1-11.
65. B. Li, Y. Yan, C. Shen, Y. Yu, Q. Wang and M. Liu, *Nanoscale*, 2018, **10**, 16217-16230.

Table of Contents



A protein-based, low-resistance Janus nanofabric is designed and fabricated for simultaneously trapping polysulfides and stabilizing lithium metal.